Pressure-Modulated Conductivity, Carrier Density, and Mobility of Multilayered Tungsten Disulfide

Avinash P. Nayak,[†,#] Zhen Yuan,[‡,#] Boxiao Cao,[§] Jin Liu,[⊥] Junjie Wu,[∥] Samuel T. Moran,[†] Tianshu Li,[§] Deji Akinwande,[*,†] Changqing Jin,[‡] and Jung-Fu Lin[⊥,∥]

[†]Department of Electrical and Computer Engineering and [⊥]Department of Geological Sciences, The University of Texas at Austin, Austin, Texas 78712, United States, [‡]Beijing National Laboratory for Condensed Matter Physics, Institute of Physics, Chinese Academy of Sciences, Collaborative Innovation Center of Quantum Matt, Beijing 100190, China, [§]Department of Civil and Environmental Engineering, Computational Materials Science Group, George Washington University, 20052, Washington, D.C., United States, and [∥]Center for High Pressure Science and Advanced Technology Research (HPSTAR), Shanghai 201900, China. [#]A. P. Nayak and Z. Yuan contributed equally.

ABSTRACT Tungsten disulfide (WS_2) is a layered transition metal dichalcogenide (TMD) that differs from other two-dimensional (2D) compounds such as graphene due to its unique semiconducting, tunable-band-gap nature. Multilayered WS_2 exhibits an indirect band gap E_g of ~1.3 eV, along with a higher load-bearing ability that is promising for strain-tuning device applications, but the electronic properties of multilayered WS_2 at higher strain conditions (*i.e.*, static strain >12%) remain an open question. Here we have studied the structural, electronic, electrical, and vibrational properties of multilayered WS_2 at hydrostatic pressures up to ~35 GPa experimentally in a diamond anvil cell and theoretically using first-principles *ab initio* calculations. Our results show that WS_2 undergoes an isostructural semiconductor-to-metallic (S−M) transition at approximately 22 GPa at 280 K, which arises from the overlap of the highest valence and lowest conduction bands. The S−M transition is caused by increased sulfur−sulfur interactions as the interlayer spacing decreases with applied hydrostatic pressure. The metalization in WS_2 can be alternatively interpreted as a 2D to 3D (three-dimensional) phase transition that is associated with a substantial modulation of the charge carrier characteristics including a 6-order decrease in resistivity, a 2-order decrease in mobility, and a 4-order increase in carrier concentration. These distinct pressure-tunable characteristics of the dimensionalized WS_2 differentiate it from other TMD compounds such as MoS_2 and promise future developments in strain-modulated advanced devices.

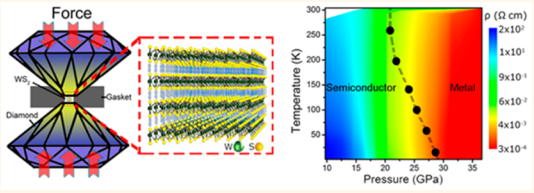

KEYWORDS: transition metal dichalcogenides · 2D materials · pressure engineering · strain · diamond anvil cell

Owing to the rich two-dimensional character of the transition metal dichalcogenides (TMDs), interest in both the electronic and structural aspects of these materials has been growing rapidly.[1−4] TMDs afford a variety of electronic states, such as superconducting,[5] semiconducting, and metallic states,[3,6] in addition to exhibiting a Mott transition[7] and Anderson localization phenomena.[8] By changing the level of interaction in the multilayered TMDs, as in our previous study, we have shown the emergence of an isostructural semiconductor to metal (S−M) transition in MoS_2 that is associated with significant changes in vibrational, optical, electrical, transport, and elastic properties.[6,9] Of the semiconducting TMD materials, tungsten disulfide (WS_2) has attracted significant interest due to its unique structural,[10] optical,[11,12] thermal,[13] and electronic[14] properties. Unlike monolayer graphene, which has sp^2 hybridization, multilayered semiconducting WS_2 has an indirect band gap E_g of ~1.3 eV. Similar to other TMDs such as MoS_2, WS_2 is a layered TMD in the hexagonal crystal structure, in which tungsten has a trigonal prismatic coordination to sulfur, and strong in-plane covalent bonds exist between the transition metal (W) and the two chalcogen (S) atoms, while weak out-of-plane van der Waals (vdW) forces exist interstitially between layers. Since the out-of-plane atoms along the *c*-axis are interacting *via* weak vdW forces, compression is easier along this axis in comparison to the covalently bonded basal plane. This has therefore enabled experimental preparation of WS_2 by means of mechanical exfoliation for fundamental studies. Applying hydrostatic pressure allows for control over the vdW interlayer spacing and therefore affords modulation of the electronic properties.

* Address correspondence to deji@ece.utexas.edu.

Received for review June 2, 2015 and accepted August 10, 2015.

Published online August 10, 2015
10.1021/acsnano.5b03295

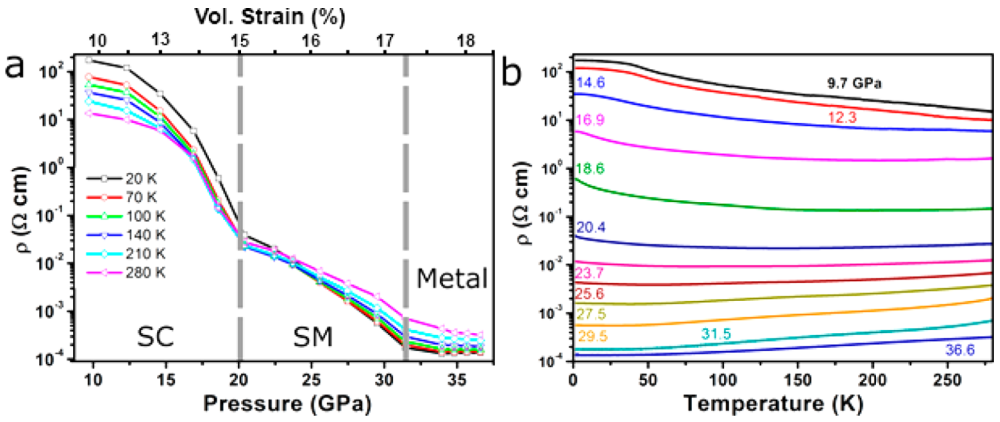

Figure 1. Pressure-induced metalization of the multilayered WS_2. (a) Electrical resistivity (ρ) as a function of pressure at representative temperatures. The results show a resistivity reduction by 6 orders of magnitude, leading to a gradual metalization from the semiconducting (SC) to the semimetallic (SM) state at approximately 20 GPa, while the metallic state (Metal) completely occurs at above ~32 GPa. (b) Temperature-dependent resistivity at each given pressure. The change in the dρ/dT slope from negative to positive is used to ascertain the transition from the semiconducting to the metallic state, respectively.

Along with its higher density and molecular weight, the load-bearing ability of WS_2 is higher than that of MoS_2. These properties of WS_2 allow for pressure or strain engineering, offering a degree of control in tuning the structure−property relations of the layered nanomaterials that can be exploited in advanced optical switches,[15] sensors,[16] and mobility engineering of transistor devices.[17]

Experimentally, to modify the electronic properties of WS_2, several methods, including intercalation,[18] layer confinement,[19] chemical vapor growth,[20−22] dual gating,[17] and strain[23] have been explored. From a theoretical viewpoint, several studies have concentrated their efforts on strain (*i.e.*, uniaxial or biaxial strain) engineering of the electronic properties of WS_2,[10,24,25] uncovering several phenomena such as strain-induced direct-to-indirect band gap (D-to-I) transition[9] and semiconductor-to-metallic (S−M) transition.[24,26] Compared to these methods, applying hydrostatic pressure permits studies of larger mechanical effects on the structural and electronic properties.

Despite theoretical studies[24] suggesting metalization of multilayered WS_2, no experimental evidence for such a transition has surfaced until now. In this study, using a diamond anvil cell (DAC) apparatus (Figure S1a), we examine the gradual S−M transition of WS_2 up to ~35 GPa. With a 6-order decrease in resistivity, semiconducting WS_2 metalizes at ~22 GPa at room temperature, while a 4-order increase in carrier concentration is observed. Along with the experimental evidence, first-principles *ab initio* theoretical calculations augment the experimental results to clearly elucidate the underlying physics responsible for the S−M transition and the increase in the carrier concentration. The electronic changes observed in carrier density and mobility for the first time are discussed in terms of their relevance to the metalization and sulfur−sulfur interactions. The continuous tuning of the optical, structural, and electronic states provides a platform for developing pressure-modulated electronics or pressure-tronics for future material technologies.

RESULTS AND DISCUSSION

The electronic transport measurements over the range of ~35 GPa reveal the tunability of the material properties of WS_2. Standard four-point probe *in situ* electrical resistivity measurements were conducted in a DAC (Figure S1b). Under hydrostatic pressure, the measured electrical resistivity (ρ) shows a gradual decrease with increasing pressure and ultimately undergoes a metalization at pressures above 22 GPa at 280 K (Figure 1a). Our results show that the semiconducting (SC) to metal (M) transition occurs over a broad pressure−temperature range that is intermediate between the two states. The resistivity profiles at different pressures are similar for various temperatures but vary in resistance values owing to thermally activated carriers.[27] To uncover the semiconducting and metallic behavior of WS_2 at high pressures, the resistivity of the sample is measured as a function of temperature to as low as 2 K. The temperature-dependent resistivity profile shows that at pressures lower than approximately 22 GPa a negative dρ/dT is observed, indicating the presence of a semiconducting state. At pressures above 22 GPa, a positive dρ/dT is observed, reflective of a metallic state in the multilayered WS_2 (Figure 1b). Although we do not find evidence of a pressure-induced superconducting state up to ~35 GPa at 2 K, applying hydrostatic pressure onto multilayered WS_2 shows a 6-order magnitude tunability of the electrical resistivity from the semiconducting to metallic state.

Analysis of the pressure-dependent resistivity profile at representative pressures and temperatures shows that the S−M transition occurring at a range of 23−28 GPa exhibits a negative transition boundary (Figure 2a). At 290 K, the electrical resistivity decreases gradually

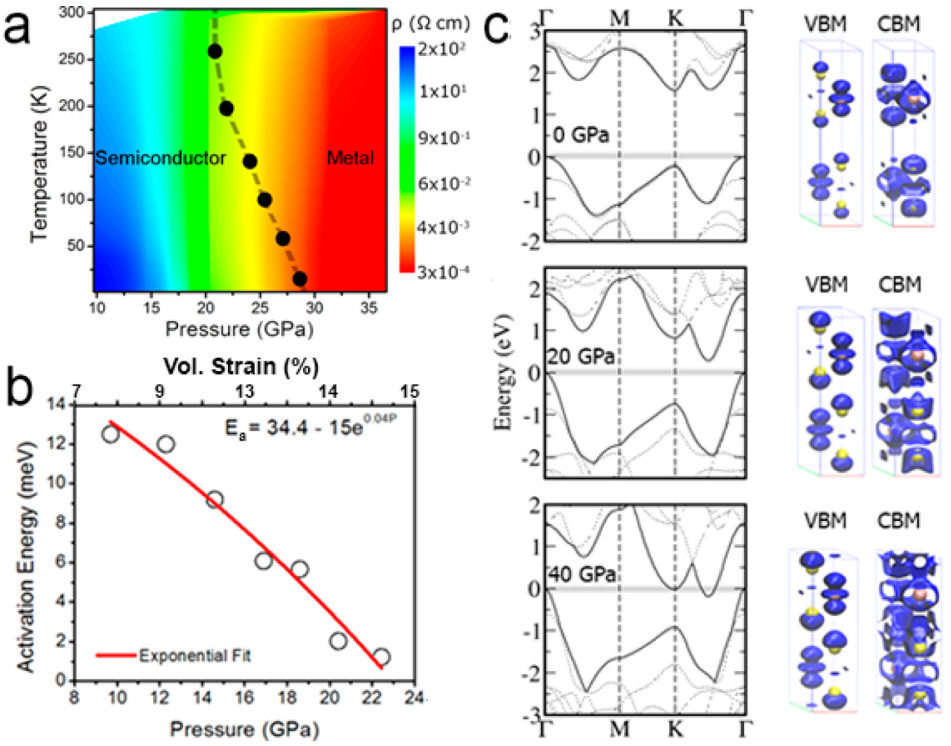

Figure 2. Metalization mechanism of the multilayered WS_2 as a function of hydrostatic pressure. (a) Temperature−pressure contour plot of resistivity showing the transition region from the semiconductor to metallic region that is derived from experimental electrical conductivity measurements in a DAC. The dashed line is plotted to highlight the onset of metalization transition as well as the overall transition boundary that exhibits a negative slope between the semiconducting and the metallic state. (b) Arrhenius plot showing the activation energy exponentially decreases with pressure, indicating the occurrence of the metallic state at pressures above ∼22 GPa. Estimates of the activation energy are obtained using ln $R \propto E_a/2k_BT$ in the temperature range between 50 and 100 K, where R is the electrical resistance, k_B is Boltzmann's constant, and E_a is the activation energy. (c) Theoretical band structure diagrams at the M, K, and Γ symmetry points at three representative pressures of 0, 20.4, and 39.5 GPa depicting the closure of the band gap. The charge densities at the VBM and CBM increase in interlayer interactions; at 39.5 GPa, the electrons are shown to cross the Fermi level, suggesting a complete metalization.

by 6 orders of magnitude from 2×10^2 Ωcm at 10 GPa to 3×10^{-4} Ωcm at 36 GPa. Unlike the abrupt drop in ρ for MoS_2 in our previous study,[6] a gradual decrease in ρ is observed in WS_2, which suggests the gradual tunability of the electronic structure and band gap. It is notable that the minimum resistivity observed here (3×10^{-4} Ωcm at 36 GPa) is comparable to the resistivity ($\sim 10^{-4}$ Ωcm) of semimetallic or metallic TMDs under ambient conditions.[3] To understand the S−M dependence on the transition metal (W or Mo), we compare the optical and electronic structure of WS_2 and MoS_2 (Figure S2). The band diagrams of the bulk WS_2 and MoS_2 are similar and show an indirect band gap of ∼1.3 eV at ambient pressure. Experimentally, multilayered WS_2 metalizes at ∼22 GPa, in comparison to multilayered MoS_2, which metalizes at ∼19 GPa at room temperature. *In situ* X-ray diffraction (XRD) shows that the in-plane compression and out-of-plane compression for MoS_2 are more than those for WS_2, which implies that the pressure effects are more prominent on MoS_2 than WS_2. To understand the differences between the two TMDs, we measure the Raman-pressure dependence (cm^{-1}/GPa), transition pressure, and the resistivity (ρ) in the semiconducting and metallic region (Figure S2).

The extracted activation energy depends on pressure as shown in Figure 2b, which can be analytically modeled as $E_a = 34.4 - 15e^{0.04P}$ where E_a is the thermal activation energy (in meV) and P is pressure (in GPa). The effective defect energy level in the band gap that typically contributes mobile carriers is directly related to the activation energy, and as the band gap closes, the activation energy approaches zero. The good agreement between the activation energy and the onset of metalization (denoted by the semimetallic region in Figure 1a) indicates that the increased charge transport in WS_2 is pressure activated. Further application of pressure beyond ∼22 GPa is attributed to intrinsic band closure and complete metalization (denoted by the metallic region in Figure 1a). The pressure at which metalization occurs is heavily dependent on the number of layers present. From our previous work,[6] we speculate that the pressure of metalization decreases with an increase in the number of WS_2 layers. Theoretical calculations also confirm the closure of the multilayered WS_2 band gap with applied hydrostatic pressure (Figure 2c). Beyond 32 GPa, the valence band maxima (VBM) and the conduction band minima (CBM) cross the Fermi level, indicating

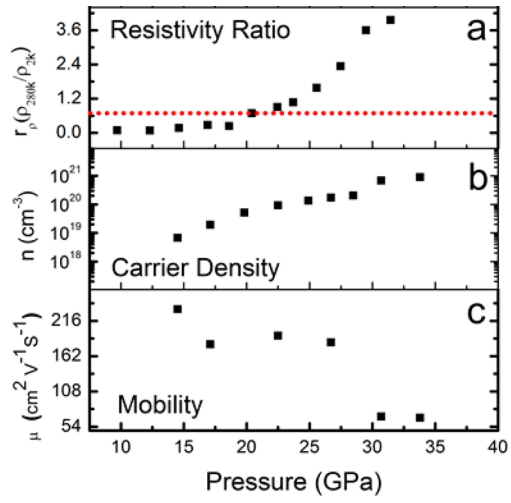

Figure 3. Electronic carrier dynamics of the multilayered WS_2 as a function of pressure. (a) The resistivity ratio (r_ρ) at pressures above 22 GPa is > 1, which signifies the onset of metalization, whereas r_ρ < 1 is observed at lower pressures. The red line indicates the electronic transition between the semiconducting and the metallic state. (b) The carrier density increases by approximately 2 orders of magnitude from 10^{19} cm^{-3} at 15 GPa to 10^{21} cm^{-3} at 35 GPa in the semiconductor and metallic regions, respectively. (c) The Hall mobility decreases by 2 orders of magnitude, indicating the prominent effect of the interlayer scattering.

a complete metalization past this pressure point. With increasing pressure, both the VBM and CBM shift their energy levels due to the increased interlayer electronic coupling, similar to the case of MoS_2.[6] The VBM is contributed from the combination of both the antibonding p_z orbitals on S atoms and the d_{z^2} orbitals from W atoms. With increasing pressure, the energy level of the VBM shifts significantly upward.[28] The CBM, which is also partially composed of the bonding p_z orbitals from S, shifts its energy downward due to the increased overlap upon the decrease of the interlayer distance (Figure S3).

In order to probe charge transport under pressure, Hall effect measurements were conducted with a magnetic field (*H*) perpendicular to the *a*–*b* plane of the single-crystal WS_2 and the H was swept as a function of pressure at three given temperatures of 2, 130, and 290 K, respectively (Figure S4). These results allow us to derive the Hall coefficients and resistivity of WS_2 at high pressures.[29,30] A gradual increase in the conductivity is observed, which can be understood by the increase in interlayer interactions, and is consistent with our theoretical results and prior reports on multilayered MoS_2 with increasing hydrostatic pressure.[6,28,31] The effect that the structural perturbation has on electron transport can be quantified by the resistivity ratio r_ρ, defined as $\rho_{280\ K}/\rho_{2K}$.[7] The transition of the resistivity ratio r_ρ from values smaller than 1 to values larger than 1 is indicative of the onset of metalization (Figure 3a). The carrier density increases with applied pressure (Figure 3b), showing approximately a 2-order magnitude increase in carrier density at 15 GPa compared to 35 GPa. In comparison to the reported carrier density at room ambient pressure, the carrier density at 35 GPa in this work demonstrates about 4 orders of magnitude of tunability.[16] *Ab initio* calculations also show that the densities of state increase with pressure, and this increase in carrier density is associated with the $d_{x^2-y^2}$ orbital contributing significantly to the carrier concentration in multilayered WS_2. The Hall measurements also permit us to evaluate the Hall carrier mobility, in which a decrease from ~240 $cm^2\ V^{-1}\ s^{-1}$ in the semiconducting region to ~60 $cm^2\ V^{-1}\ s^{-1}$ in the metallic region is observed (Figure 3c). We note that a recent report on a high-mobility multilayer WS_2 transistor gave an estimate of the field-effect mobility of ~90 $cm^2\ V^{-1}\ s^{-1}$ at room temperature.[16] The decrease in the mobility of WS_2 in the metallic phase is due to the pressure-induced doping when the free carriers scatter within the confined lattice more frequently, therefore resulting in a decrease in drift velocity.[32] The mobility reported in this work is the Hall mobility, a measure of the intrinsic carrier mobility, and is typically higher than the field-effect mobility, which suffers from additional transport effects such as gate–oxide interface scattering and contact resistance.[33,34]

Electronic transitions are usually accompanied by crystal structural distortions or transformations. For many pressure-induced structural phase transitions, *in situ* XRD can be used to decipher the structure modification. For pressure-induced isostructural phase transition, analysis of the bulk and axial incompressibility may allow further understanding of the driving forces of high-pressure phase transitions. Refinements of the XRD patterns of the sample show that it remains isostructural across the metalization transition (Figure 4a). Although the pressure–volume relation of the multilayered WS_2 does not display a sudden drop across the metalization transition at approximately 22 GPa, analysis of the compression data using a third-order Birch–Murnaghan (BM) equation of state (EOS) shows that the metallic state exhibits a distinct EOS behavior from that of the semiconducting state (Figure 4a). Furthermore, the linear compressibility of the out-of-plane *c*-axis is much higher than that of the in-plane *a*-axis in the semiconducting state at pressures up to 22 GPa, bringing WS_2 layers closer to each other, which eventually leads to enhanced sulfur–sulfur interactions and resulting metalization. On the other hand, the axial compressibility of the metallic state does not show a distinct difference between the *a*- and *c*-axes. Although we do not observe a structural distortion up to 35 GPa, it has been suggested that further pressure increase could lead to layer sliding from the stable $2H_a$ phase to the $2H_c$ phase at high pressure.[35]

To elucidate the structural distortion and changes in the electronic states, Raman spectroscopy can be used and has proven to be a powerful tool in determining

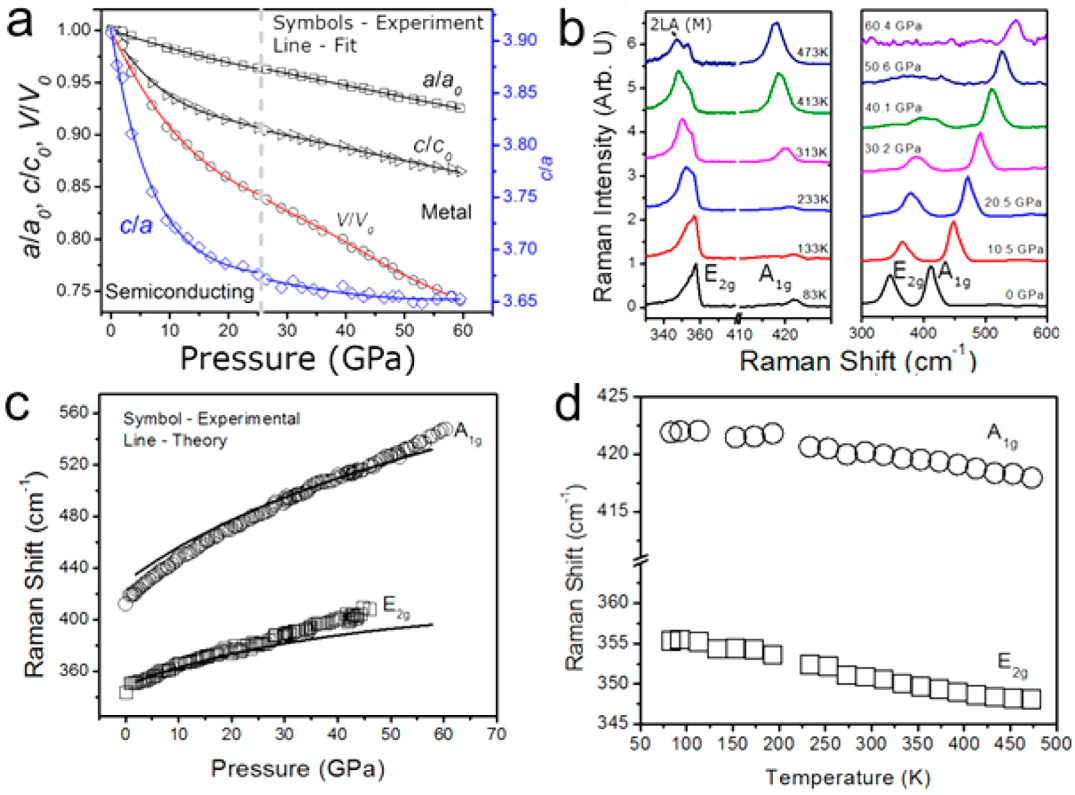

Figure 4. Structural and vibrational properties of the multilayered WS_2 under high pressure. (a) *In situ* XRD showing that the sample remains in the hexagonal structure up to 60 GPa. The *c*-axis is more compressible than the *a*-axis at pressures below approximately 22 GPa but becomes much less compressible at pressures higher than 22 GPa, where the metalization occurs. The dashed gray line shows the S−M transition pressure at ~22 GPa and 280 K. (b) Raman spectra for selected temperatures and pressures showing that with increasing temperature, the A_{1g} mode becomes more prominent while the 2LA(M) is suppressed (left panel). Moreover, hydrostatic pressure suppresses the E_{2g} mode (right panel). (c) Pressure-dependent Raman shifts showing a phonon hardening for both the E_{2g} and A_{1g} modes. The solid lines are the theoretical calculation, which are in good agreement with experimental results. (d) Temperature-dependent Raman shifts indicating a phonon softening at a rate of −0.02 and −0.01 cm^{-1}/K for the E_{2g} and A_{1g} modes, respectively.

information on the number of layers,[36] doping concentration,[37] and strain effect[2] in TMDs. Here we have investigated the vibrational modes of WS_2 with varying pressure and temperature. Selected pressure and temperature Raman profiles show phonon hardening as well as E_{2g} mode suppression at high pressures (Figure 4b), which has also been observed in other TMDs.[6,38] Suppression of the intensity ratio between the A_{1g} and E_{2g} modes decreases with pressure (Figure S5a), and the suppressed E_{2g} mode is associated with broadening of the FWHM at higher pressures (Figure S5b). At higher temperatures, the 2LA(M) mode is more prominent (Figure 4b) and the FWHM is observed to increase with temperature for all Raman modes (Figure S5c). The intensity ratio between the two Raman modes has also been shown to decrease with an increase in temperature (Figure S5d). At lower temperatures, there is overlap between the 2LA(M) and E_{2g} modes, and only one integral peak is observed. The pressure-dependent Raman shows the A_{1g} mode being prominent at high pressures, while the E_{2g} mode is suppressed (Figure 4c). The temperature-dependent Raman, however, indicates phonon softening (Figure 4d) at a rate of −0.02, −0.01, and −0.01 cm^{-1}/K for the 2LA(M), E_{2g}, and A_{1g} modes, respectively. In comparison to its monolayer counterpart,[39] an order of magnitude difference in the softening rate is observed in multilayered WS_2. We attribute the difference to the double resonance scattering that is present only in monolayer WS_2.[21]

CONCLUSION

In summary, we have applied hydrostatic strain as high as 18% to multilayered WS_2 in a high-pressure DAC coupled with electrical (Hall measurements), vibrational, and structural investigations up to approximately 35 GPa. Together with DFT calculations, our results reveal the band gap closure of the multilayered WS_2 that is predominantly modulated *via* increasing interlayer interactions and sulfur−sulfur interactions at pressures above 22 GPa (15% volume strain), leading to dramatically enhanced conductivity and carrier density while the mobility is drastically reduced. This metallic WS_2 occurs at a higher pressure than that of the multilayered MoS_2 and can be understood here in terms of the layer tuning effect on the electronic and

transport properties of the TMD compounds. These results on the electronic structures and carrier density and mobility of strain-tuned WS_2 lead to a better understanding of the multilayered TMDs under high strains and promise future developments in strain-modulated advanced devices. At higher pressures than in this study, it is conceivable that a superconducting state in WS_2 may occur similar to recent very high pressure investigations in multilayered MoS_2.[31]

METHODS

High-Pressure Laser Raman Spectroscopy. The Raman spectra were recorded with a Renishaw Micro-Raman spectroscopy system (Renishaw PLC, Gloucestershire, UK) with a laser wavelength of 532 nm, spectral resolution of ~1 cm^{-1}, and focus laser spot on the sample of ~1 μm with an output power of 100 mW. High-pressure Raman experiments were performed using a symmetric diamond anvil cell with silicone oil as the pressure-transmitting medium. The WS_2 single-crystal sample was purchased from 2D Semiconductors. The purity of the crystals was characterized and estimated to be greater than 99% by 2D Semiconductors. The crystal was placed in a T301 stainless-steel gasket chamber with a diameter of 125 μm and a thickness of 30 μm. Ruby spheres were loaded close to the sample in the sample chamber of the DAC simultaneously as the pressure calibrant. Pressure was measured based on the shifts of the ruby R_1 and R_2 fluorescence lines.[40] Considering that silicone oil was added as a pressure medium, the estimated pressure errors are ~0.5 GPa at pressures less than 10 GPa and ~1 GPa at higher pressures.

High-Pressure Electrical Resistance Measurements. The resistance measurement of the WS_2 single-crystal sample under high pressure was conducted using the standard four-point-probe electrical technique in a screw-type DAC made of BeCu alloy. To measure the resistivity as a function of temperature of the WS_2 single-crystal sample, the DAC was put inside a Mag Lab system upon loading. The temperature was automatically program controlled *via* the Mag Lab system. The diamond was 300 μm in diameter, with a flat center and an 8 degree bevel out to 500 μm. A T301 stainless steel gasket was preindented from a thickness of 250 μm to 40 μm, and a hole was drilled at the center with a diameter of 100 μm. Fine cubic boron nitride (c-BN) powders were used to cover the gasket to keep the electrode leads insulated from the metallic gasket as an insulating layer. The c-BN powders were pressed and further drilled into the center chamber. A WS_2 single crystal with dimensions of 40 μm × 50 μm × 5 μm was loaded into the sample chamber, together with three ruby spheres as the pressure calibrant and four slim gold wires (18 um) used as electrodes for the electrical resistance measurements. The soft cubic boron nitride (hBN) fine powder surrounded the center chamber as the pressure-transmitting medium.

The high-pressure Hall effects were measured based on the van der Pauw method using a piston cylinder-type instrument that was inserted into the Mag Lab system.

Theoretical Calculations. Theoretical calculations were carried out using the Vienna Ab Initio Simulation Package (VASP)[41−43] based on the Perdew−Burke−Ernzerhof (PBE) functional[44] and the projector augmented wave method.[45,46] A Monkhorst−Pack k-point mesh of 17 × 17 × 5 was used to sample the first Brillouin zone, and the plane wave cutoff was set to be 950 eV. The ions were relaxed by a quasi-Newton algorithm while keeping the unit cell volume fixed, and the pressure was calculated after relaxation. The convergence criteria were 10^{-6} eV and 10^{-5} eV per unit cell for electronic and ionic relaxations, respectively. In Raman spectrum calculations, the Hessian matrix was calculated using the finite difference method; each ion was displaced 0.015 Å in each direction from its equilibrium position, and the Hessian matrix was calculated from the calculated force constants. The vibrational frequencies were calculated from eigenvalues of the Hessian matrix.

Conflict of Interest: The authors declare no competing financial interest.

Supporting Information Available: The Supporting Information is available free of charge on the ACS Publications website at DOI: 10.1021/acsnano.5b03295.

Comparison of MoS_2 and WS_2, the carrier density measurements at different temperatures and pressures, and the diamond anvil cell setup (PDF)

Acknowledgment. Research at The University of Texas at Austin was supported in part by a Young Investigator Award (D.A.) from the Defense Threat Reduction Agency (DTRA) and the Office of Naval Research (ONR). Research at the Chinese Academy of Sciences was supported by the National Science Foundation (NSF) and Ministry of Science and Technology (MOST) of China through research projects. J.F.L. acknowledges financial support from the Center for High Pressure Science and Advanced Technology Research (HPSTAR). We also thank J. Wozniak and Texas Advanced Computing Center (TACC) for their help with the 3D rendering. We also acknowledge Megan Matheney for her careful review of the manuscript.

REFERENCES AND NOTES

1. Wang, Q. H.; Kalantar-Zadeh, K.; Kis, A.; Coleman, J. N.; Strano, M. S. Electronics and Optoelectronics Of Two-Dimensional Transition Metal Dichalcogenides. *Nat. Nanotechnol.* **2012**, *7*, 699–712.
2. Akinwande, D.; Petrone, N.; Hone, J., Two-Dimensional Flexible Nanoelectronics. *Nat. Commun.* **2014**, *5*.5678
3. Chhowalla, M.; Shin, H. S.; Eda, G.; Li, L.-J.; Loh, K. P.; Zhang, H. The Chemistry Of Two-Dimensional Layered Transition Metal Dichalcogenide Nanosheets. *Nat. Chem.* **2013**, *5*, 263–275.
4. Chang, H.-Y.; Yang, S.; Lee, J.; Tao, L.; Hwang, W.-S.; Jena, D.; Lu, N.; Akinwande, D. High-Performance, Highly Bendable MoS2 Transistors with High-K Dielectrics for Flexible Low-Power Systems. *ACS Nano* **2013**, *7*, 5446–5452.
5. Castro Neto, A. H. Charge Density Wave, Superconductivity, and Anomalous Metallic Behavior in 2D Transition Metal Dichalcogenides. *Phys. Rev. Lett.* **2001**, *86*, 4382–4385.
6. Nayak, A. P.; Bhattacharyya, S.; Zhu, J.; Liu, J.; Wu, X.; Pandey, T.; Jin, C.; Singh, A. K.; Akinwande, D.; Lin, J.-F., Pressure-Induced Semiconducting To Metallic Transition In Multilayered Molybdenum Disulphide. *Nat. Commun.* **2014**, *5*.10.1038/ncomms4731
7. Siegrist, T.; Jost, P.; Volker, H.; Woda, M.; Merkelbach, P.; Schlockermann, C.; Wuttig, M. Disorder-Induced Localization in Crystalline Phase-Change Materials. *Nat. Mater.* **2011**, *10*, 202–208.
8. Thouless, D. Anderson Localization in the Seventies and Beyond. *Int. J. Mod. Phys. B* **2010**, *24*, 1507–1525.
9. Nayak, A. P.; Pandey, T.; Voiry, D.; Liu, J.; Moran, S. T.; Sharma, A.; Tan, C.; Chen, C.-H.; Li, L.-J.; Chhowalla, M.; et al. Pressure-Dependent Optical and Vibrational Properties of Monolayer Molybdenum Disulfide. *Nano Lett.* **2015**, *15*, 346.
10. Duerloo, K.-A. N.; Li, Y.; Reed, E. J., Structural Phase Transitions In Two-Dimensional Mo- And W-Dichalcogenide Monolayers. *Nat. Commun.* **2014**, *5*.10.1038/ncomms5214
11. Jo, S.; Ubrig, N.; Berger, H.; Kuzmenko, A. B.; Morpurgo, A. F. Mono- and Bilayer WS_2 Light-Emitting Transistors. *Nano Lett.* **2014**, *14*, 2019–2025.
12. He, J.; Kumar, N.; Bellus, M. Z.; Chiu, H.-Y.; He, D.; Wang, Y.; Zhao, H. Electron Transfer and Coupling in Graphene−Tungsten

Disulfide van der Waals Heterostructures. *Nat. Commun.* **2014**, *5*, 5622
13. Gandi, A. N.; Schwingenschlögl, U. WS_2 As an Excellent High-Temperature Thermoelectric Material. *Chem. Mater.* **2014**, *26*, 6628–6637.
14. Ovchinnikov, D.; Allain, A.; Huang, Y.-S.; Dumcenco, D.; Kis, A. Electrical Transport Properties of Single-Layer WS_2. *ACS Nano* **2014**, *8*, 8174–8181.
15. Tsai, D.-S.; Liu, K.-K.; Lien, D.-H.; Tsai, M.-L.; Kang, C.-F.; Lin, C.-A.; Li, L.-J.; He, J.-H. Few-Layer MoS_2 with High Broadband Photogain and Fast Optical Switching for Use in Harsh Environments. *ACS Nano* **2013**, *7*, 3905–3911.
16. Iqbal, M. W.; Iqbal, M. Z.; Khan, M. F.; Shehzad, M. A.; Seo, Y.; Eom, J. Deep-Ultraviolet-Light-Driven Reversible Doping Of WS_2 Field-Effect Transistors. *Nanoscale* **2015**, *7*, 747–757.
17. Radisavljevic, B.; Kis, A. Mobility Engineering and a Metal–Insulator Transition In Monolayer MoS_2. *Nat. Mater.* **2013**, *12*, 815–820.
18. Ohuchi, F. S.; Jaegermann, W.; Pettenkofer, C.; Parkinson, B. A. Semiconductor To Metal Transition Of WS_2 Induced By K Intercalation In Ultrahigh Vacuum. *Langmuir* **1989**, *5*, 439–442.
19. Georgiou, T.; Yang, H.; Jalil, R.; Chapman, J.; Novoselov, K. S.; Mishchenko, A. Electrical and Optical Characterization Of Atomically Thin WS_2. *J. Chem. Soc., Dalton Trans.* **2014**, *43*, 10388–10391.
20. Yen, P. C.; Huang, Y. S.; Tiong, K. K. The Growth And Characterization Of Rhenium-Doped WS_2 Single Crystals. *J. Phys.: Condens. Matter* **2004**, *16*, 2171.
21. Gutiérrez, H. R.; Perea-López, N.; Elías, A. L.; Berkdemir, A.; Wang, B.; Lv, R.; López-Urías, F.; Crespi, V. H.; Terrones, H.; Terrones, M. Extraordinary Room-Temperature Photoluminescence in Triangular WS_2 Monolayers. *Nano Lett.* **2013**, *13*, 3447–3454.
22. Chen, Y.; Xi, J.; Dumcenco, D. O.; Liu, Z.; Suenaga, K.; Wang, D.; Shuai, Z.; Huang, Y.-S.; Xie, L. Tunable Band Gap Photoluminescence from Atomically Thin Transition-Metal Dichalcogenide Alloys. *ACS Nano* **2013**, *7*, 4610–4616.
23. Voiry, D.; Yamaguchi, H.; Li, J.; Silva, R.; Alves, D. C. B.; Fujita, T.; Chen, M.; Asefa, T.; Shenoy, V. B.; Eda, G.; et al. Enhanced Catalytic Activity In Strained Chemically Exfoliated WS_2 Nanosheets For Hydrogen Evolution. *Nat. Mater.* **2013**, *12*, 850–855.
24. Bhattacharyya, S.; Singh, A. K. Semiconductor-metal Transition in Semiconducting Bilayer Sheets of Transition-metal Dichalcogenides. *Phys. Rev. B: Condens. Matter Mater. Phys.* **2012**, *86*, 075454.
25. Amin, B.; Kaloni, T. P.; Schwingenschlogl, U. Strain Engineering of WS_2, WSe_2, and WTe_2. *RSC Adv.* **2014**, *4*, 34561–34565.
26. Scalise, E.; Houssa, M.; Pourtois, G.; Afanas'ev, V.; Stesmans, A. Strain-Induced Semiconductor To Metal Transition In The Two-Dimensional Honeycomb Structure Of MoS_2. *Nano Res.* **2012**, *5*, 43–48.
27. Streetman, B. G. *Solid State Electronic Devices*; Pearson Education, Limited, 1972.
28. Cao, B.; Li, T. Interlayer Electronic Coupling in Arbitrarily Stacked MoS_2 Bilayers Controlled by Interlayer S–S Interaction. *J. Phys. Chem. C* **2015**, *119*, 1247–1252.
29. van der Pauw, L. J. A Method of Measuring Specific Resistivity and Hall Effect of Discs of Arbitrary Shape. *Philips Res. Rep.* **1958**, *13*, 1.
30. Kong, P. P.; Sun, F.; Xing, L. Y.; Zhu, J.; Zhang, S. J.; Li, W. M.; Liu, Q. Q.; Wang, X. C.; Feng, S. M.; et al. Superconductivity in Strong Spin Orbital Coupling Compound Sb_2Se_3. *Sci. Rep.* **2014**, *4*, 4.
31. Zhenhua Chi, F. Y.; Peng, F.; Zhu, J.; Zhang, Y.; Chen, X.; Yang, Z.; Liu, X.; Ma, Y.; Zhao, Y.; Kagayama, T.; Iwasa, Y. Ultrahigh Pressure Superconductivity in Molybdenum Disulfide. *Arxiv* **2015**, *1503*, 05331.
32. Harris, J. J. Delta-Doping of Semiconductors. *J. Mater. Sci.: Mater. Electron.* **1993**, *4*, 93–105.
33. Pradhan, N. R.; Rhodes, D.; Xin, Y.; Memaran, S.; Bhaskaran, L.; Siddiq, M.; Hill, S.; M. Ajayan, P.; Balicas, L. Ambipolar Molybdenum Diselenide Field-Effect Transistors: Field-Effect and Hall Mobilities. *ACS Nano* **2014**, *8*, 7923–7929.
34. Chang, H.-Y.; Zhu, W.; Akinwande, D. On The Mobility And Contact Resistance Evaluation For Transistors Based On MoS_2 Or Two-Dimensional Semiconducting Atomic Crystals. *Appl. Phys. Lett.* **2014**, *104*, 113504.
35. Hromadová, L.; Martoňák, R.; Tosatti, E. Structure Change, Layer Sliding, and Metallization in High-Pressure MoS_2. *Phys. Rev. B: Condens. Matter Mater. Phys.* **2013**, *87*, 144105.
36. Berkdemir, A.; Gutierrez, H. R.; Botello-Mendez, A. R.; Perea-Lopez, N.; Elias, A. L.; Chia, C.-I.; Wang, B.; Crespi, V. H.; Lopez-Urias, F.; Charlier, J.-C.; Terrones, H.; Terrones, M. Identification of Individual and Few Layers of WS_2 Using Raman Spectroscopy. *Sci. Rep.* **2013**, *3*.10.1038/srep01755
37. Laskar, M. R.; Nath, D. N.; Ma, L.; Lee, E. W.; Lee, C. H.; Kent, T.; Yang, Z.; Mishra, R.; Roldan, M. A.; Idrobo, J.-C.; et al. p-Type doping of MoS_2 thin films using Nb. *Appl. Phys. Lett.* **2014**, *104*, 092104.
38. Bandaru, N.; Kumar, R. S.; Baker, J.; Tschauner, O.; Hartmann, T.; Zhao, Y.; Venkat, R. Structural Stability of WS_2 Under High Pressure. *Int. J. Mod. Phys. B* **2014**, *28*, 1450168.
39. M, T.; Late, D. J. Temperature Dependent Phonon Shifts in Single-Layer WS_2. *ACS Appl. Mater. Interfaces* **2014**, *6*, 1158–1163.
40. Mao, H.; Xu, J.; Bell, P. Calibration Of The Ruby Pressure Gauge To 800 Kbar Under Quasi-Hydrostatic Conditions. *J. Geophys. Res.* **1986**, *91*, 4673.
41. Kresse, G.; Hafner, J. *Ab initio* molecular dynamics for liquid metals. *Phys. Rev. B: Condens. Matter Mater. Phys.* **1993**, *47*, 558–561.
42. Kresse, G.; Furthmiiller, J. Efficiency of Ab-Initio Total Energy Calculations for Metals And Semiconductors Using a Plane-Wave Basis Set. *Comput. Mater. Sci.* **1996**, *6*, 15–50.
43. Kresse, G.; Furthmüller, J. Efficient iterative schemes for Ab *initio* total-energy calculations using a plane-wave basis set. *Physical Review B.* **1996**, *54*, 11169–11186.
44. Perdew, J.; Burke, K.; Ernzerhof, M. Generalized gradient approximation made simple. *Phys. Rev. Lett.* **1996**, *77*, 3865–3868.
45. Blöchl, P. E. Projector Augmented-wave Method. *Phys. Rev. B: Condens. Matter Mater. Phys.* **1994**, *50*, 17953–17979.
46. Kresse, G.; Joubert, D. From ultrasoft pseudopotentials to the projector augmented-wave method. *Physical Review B.* **1999**, *59*, 1758–1775.